



Comparative analysis of mineral mapping for hyperspectral and multispectral imagery

Kumar M Vignesh¹ · Yarrakula Kiran²

Received: 14 February 2018 / Accepted: 22 January 2020
© Saudi Society for Geosciences 2020

Abstract

The traditional approaches of mineral-mapping are time consuming and expensive process. Remote sensing is a tool to map the minerals precisely using their physical, chemical and optical properties. In the present study, Tirunelveli district in Tamil Nadu is selected to extract the abundant mineral such as Limestone using Hyperion and Landsat-8 OLI imageries. The chemical composition of the mineral is identified using scanning electron microscope (SEM) and energy dispersive X-ray spectroscopy (EDS) analysis. The spectral reflectance of minerals is characterized using analytical spectral device (ASD) field spectroradiometer. The minerals showed deep absorption in short wave infrared region from 1800 to 2500 nm. The mineral mapping in hyperspectral data is performed using various preliminary processing such as bad band removal, vertical strip removal, radiance and reflectance generation and postprocessing steps such as data dimensional reduction, endmember extraction and classification. To improve the classification accuracy, the vertical strip removal process is performed using a local destriping algorithm. Absolute reflectance of Hyperion and Landsat-8 OLI (Operational Land Imager) imageries is carried out using the FLAASH (fast line-of-sight atmospheric analysis of hypercubes) module. Spectral data reduction techniques in reflectance bands performed using minimum noise fraction method. The noiseless reflectance bands spatial data reduced by the Pixel Purity Index method in the threshold limit of 2.5 under 10,000 repetitions. The obtained reflectance imagery spectra compared with the spectral libraries such as USGS (United States Geological Survey), JPL (Jet Propulsion Laboratory) and field spectra. Endmembers of minerals are carried out using high probability score obtained from the various methods such as SAM (spectral angle mapper), SFF (spectral feature fitting) and BE (binary encoding). The mineral mapping of both imageries is carried out using a supervised classification approach. The results showed that hyperspectral remote sensing performed good results as compared to multispectral data.

Keywords Hyperion · Landsat-8 OLI · SEM · ASD spectroradiometer · FLAASH

Introduction

A mineral is represented by a chemical formula, which is typically solid and inorganic, and has a crystal arrangement (Tiwari et al. 2015). Out of 5300, 5070 known minerals have been accepted by the International Mineralogical Association (IMA)

(Panda et al. 2014). In earlier stages to mineral, identification is based on their physical and chemical properties. The traditional methods of mineral mapping and exploration need a lot of time-consuming, cost, manpower and instruments (Zhang and Du 2012). India manufactures a total of 89 minerals. There are 52 non-metallic, 4 fuel, 11 metallic and 22 minor minerals. Day by day, the illegal mining activities are increasing; to avoid illegal mining activity, identification and mapping of minerals are required with precise accuracy (Askari et al. 2018). Remote sensing is a tool for mineral identification, geology mapping, agriculture monitoring, soil mapping, soil moisture estimation, water quality monitoring, food analyzing, surveillance, oil spill detection and etc. (Yarrakula et al. 2013). Remote sensing optical sensors are mainly used to map the minerals without physical contact. The spectral range of 0.4–2.5 μm provides abundant information about many important earth-surface minerals

This article is part of the Topical Collection on *Global Sustainability through Geosciences and Civil Engineering*

✉ Yarrakula Kiran
kiran@gkciet.ac.in

¹ Vellore Institute of Technology - VIT University, Vellore, Tamil Nadu 632014, India

² Ghani Khan Chaudhury Institute of Engineering and Technology, Malda, West Bengal 732141, India

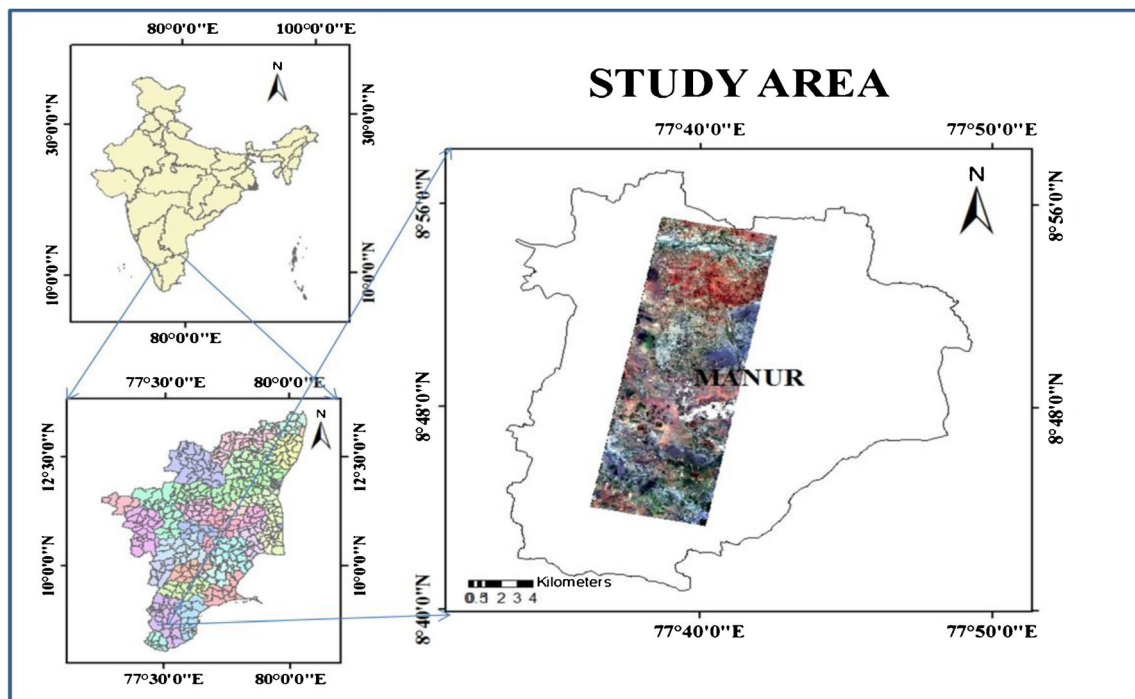


Fig. 1 Geographical position of the study area

(Kruse et al. 2003). In particular, the 2.0- to 2.5- μm (SWIR) spectral range covers spectral features of hydroxyl-bearing minerals, sulfates and carbonates common to many geologic units and hydrothermal alteration assemblages (Kruse 2003; Sheikhrasimi et al. 2019). Limestone is a type of sedimentary rock having high calcium carbonate (CaCO_3). Several of the minerals associated with calcite are easily detected using the shortwave infrared region of the spectrum (Kruse and Boardman 2000). Limestone is used in various industries like cement, steel, chemical industries such as calcium carbide, bleaching powder, soda-ash and etc. (Matar and Bamoussa 2013). In Tamil Nadu, limestone production of the mining has the waste factor around 0.26 to 1 (limestone waste). Overall, 0.3 million tonnes of mining waste already established. Normally, limestone mixed with other minerals such as dolomite, feldspar,

biotite, quartz and etc. Therefore, purest limestone mineral spectra identification for Indian condition is necessary. In future, to minimize the waste production, identifying the purest Limestone is important. The spectral characteristics of minerals obtained from spectroradiometer and spectral libraries such as USGS, JPL and JHU (Johns Hopkins University) (Noori et al. 2019). Limestone and its chemical composition spectra for Indian climatic condition are not available. The spectral libraries such as USGS, JPL and JHU are having the limestone (calcite) spectra only. Basically, every mineral shows better reflectance in short-wave infrared (SWIR) region from 1800 to 2500 nm (Kumari et al. 2014; Beiranvand Pour et al. 2018). To map the minerals using multispectral data is a simple task compared to hyperspectral sensors (Kruse and Perry 2007). In the optical sensors divided such as multispectral, hyperspectral and

Fig. 2 Limestone mineral and its spectral reflectance plot

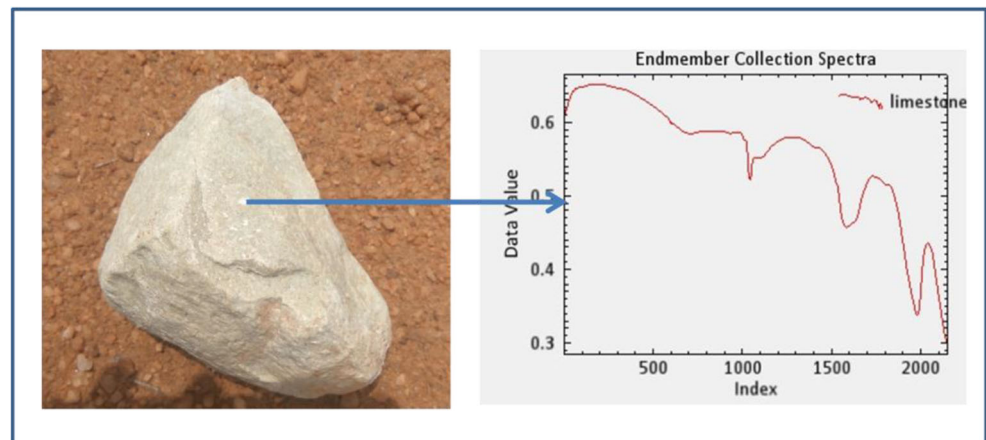


Table 1 Satellite data used and its specification

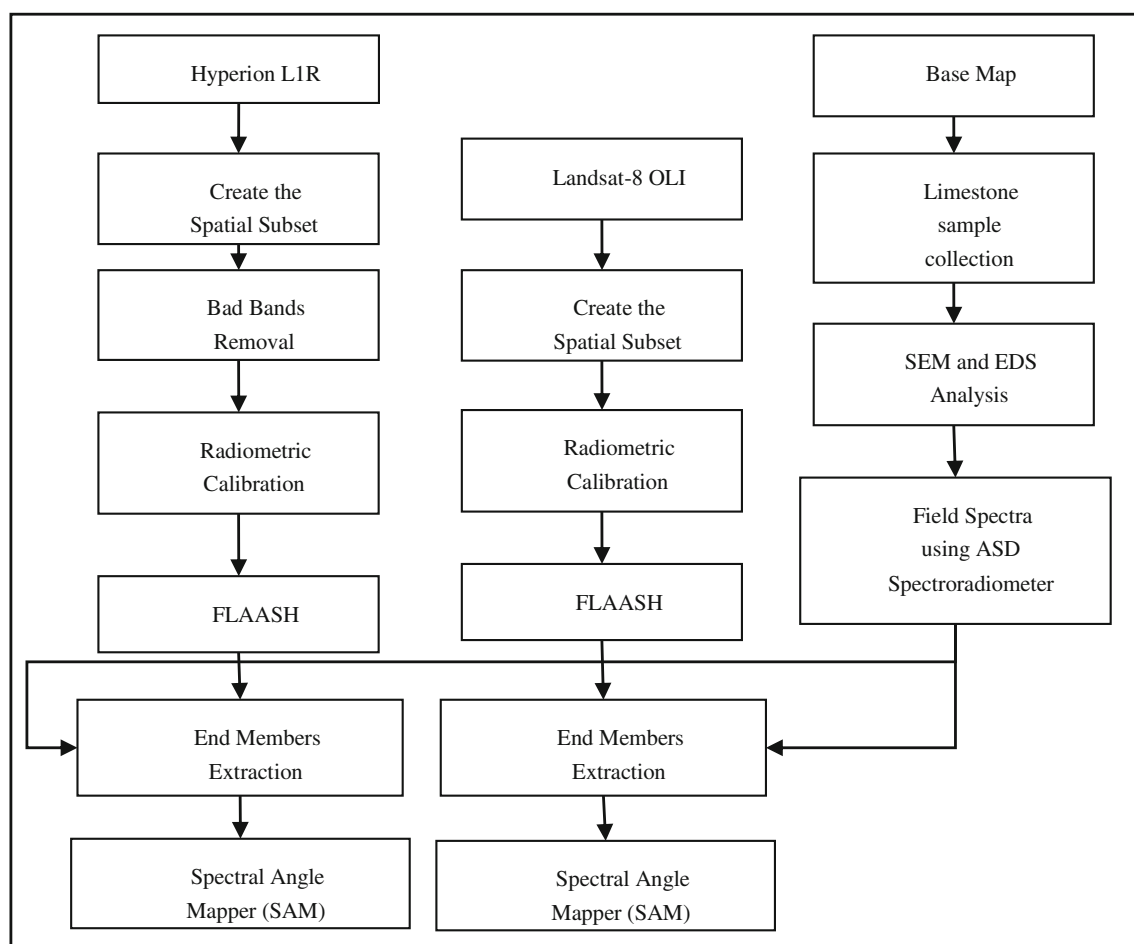
S.No	Content	Hyperion	Landsat-8 OLI
1	Number of bands	242	11
2	Spatial resolution	30 m	30 m
3	Bandwidth	Short–10 nm	Large
4	Date	2-10-2015	24-10-2015
5	Cloud cover	0–9%	0–9%

ultraspectral sensors. Multispectral datasets are mostly composed of 5 to 10 bands of relatively hefty bandwidths (70–400 nm) (Ramakrishnan et al. 2013). Hyperspectral datasets are mostly composed of 100 to 200 spectral bands of relatively short interval bandwidths (5–10 nm) (Peng 2014). Large numbers of bands provide an opportunity to identify the minerals by their corresponding spectral properties (Pour et al. 2013; Ahmadirouhani et al., 2018). Due to the fact that a large number of bands lead to complexity in processing the hyperspectral data (El-magd et al. 2014), ASTER SWIR channel groups enable key qualifications to map the different carbonate and sulfate minerals and their alteration zones. TIR groups used to execute the calcite and

quartz minerals. ALI used to identify the iron samples in VNIR wavelength range to separate a few essential ferric-press oxide minerals and SWIR groups. To extract the desired information from a large number of bands present in hyperspectral data, it needs to be processed and analyzed (Crosta and de Souza Filho, 2017). The process of hyperspectral data involves data preprocessing, atmospheric correction, data dimensionality reduction, endmembers extraction and mineral abundance estimation (Arellano et al. 2015). The main objective of the present study is to map the purest form of limestone mineral using hyperspectral and multispectral imageries and to identify the suitable optical sensor to map the minerals. Limestone spectra are developed for Indian climatic condition in the VS (400–700 nm), VNIR (700–1200 nm) and SWIR (1200–2500 nm) region.

Study area and data used

Manur block is a block of Tirunelveli district in Tamil Nadu, India. Manur block has totally 41 villages. The study area

**Fig. 3** Methodology for the limestone classification using fusion imagery

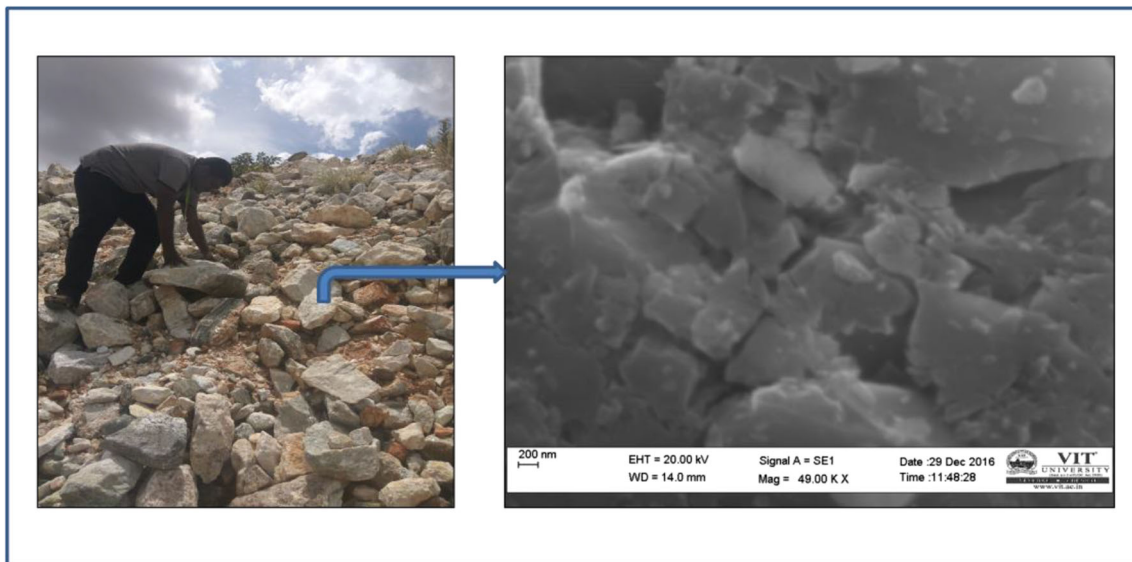


Fig. 4 High-resolution imagery of limestone identified by SEM instrument

lies in $08^{\circ} 33'12''$ to $08^{\circ} 41' 30''$ N and $77^{\circ} 34' 08''$ to $77^{\circ} 39' 39''$ E. The district is irrigated by numerous rivers such as the Pachaiyar and Tambarabarani. Figure 1 shows the geographical position of the study area. The abundant crystalline limestones are situated in parts of Tirunelveli, Ariyalur, Coimbatore, Karur, Madurai, Salem, Trichy, Tuticorin, Ramanathapuram, Nagapattinam and Virudhunagar districts of Tamil Nadu, India. The abundant non-crystalline limestones are situated in parts of Tirunelveli, Tuticorin and Trichy districts of Tamil Nadu, India.

Tirunelveli district has large mineral deposits such as limestone, wollastonite, sillimanite, kyanite, dolomite, barytes, titanium, magnesit, gypsum, garnet and granite (Renaud 2015). The study area contains big cement industries, crushing and grinding units of limestone. A major part of the area is a penepplain interspersed with small

isolated mounds. The highest elevation is 174 m near Vellankottai and the lowest elevation is around 40 m near Tamirabarani river. The area is connected by Tirunelveli to Sankaranaryanar Koil highway. The area is characterized by Quartzite and Calc Granulite with crystalline limestone of Khondalite group and Hornblende Biotite Gneiss of Peninsular Gneissic complex-II. The general trend to the litho units is NW-SE with varying dips of 40° to 50° towards the southwest. Southeasterly plunging overturned antiform is noticed in the locale. The region has large resources of crystalline limestone. It extends over a length of 2.4 km and attains a maximum width of 6.3 km with an average width of about 0.3 km. The massive limestone band varies in grain size from fine to coarse. Based on the estimated limestone resource of 14 million tonnes, a cement factory and chemical industries

Fig. 5 EDS graph and other elements present of limestone mineral

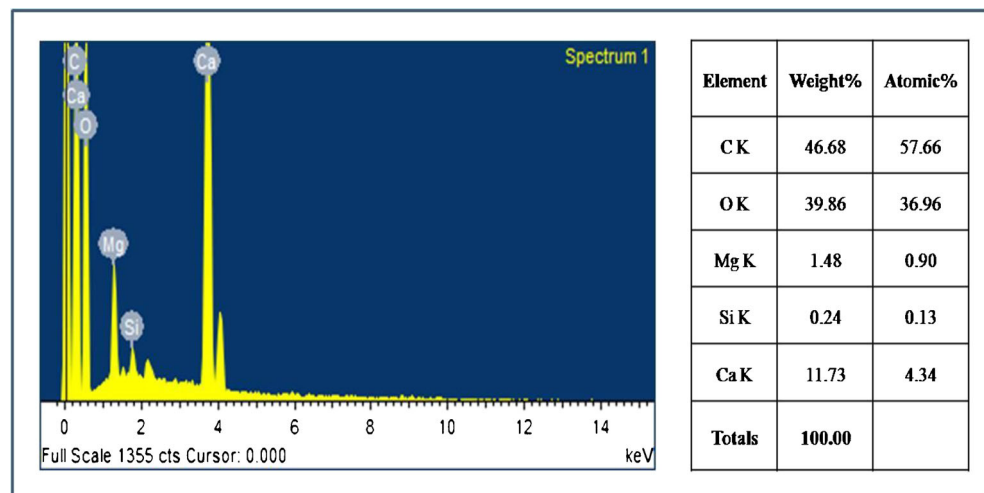
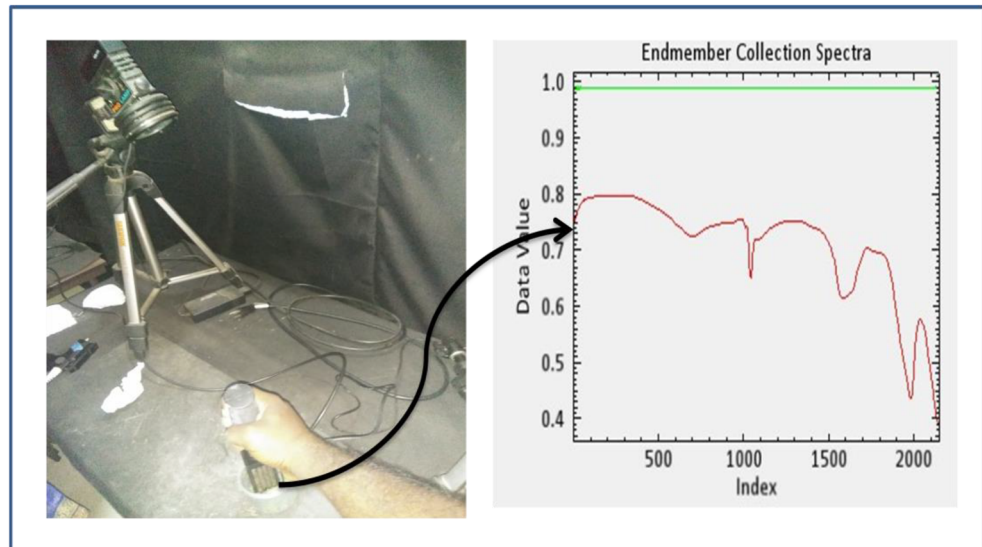
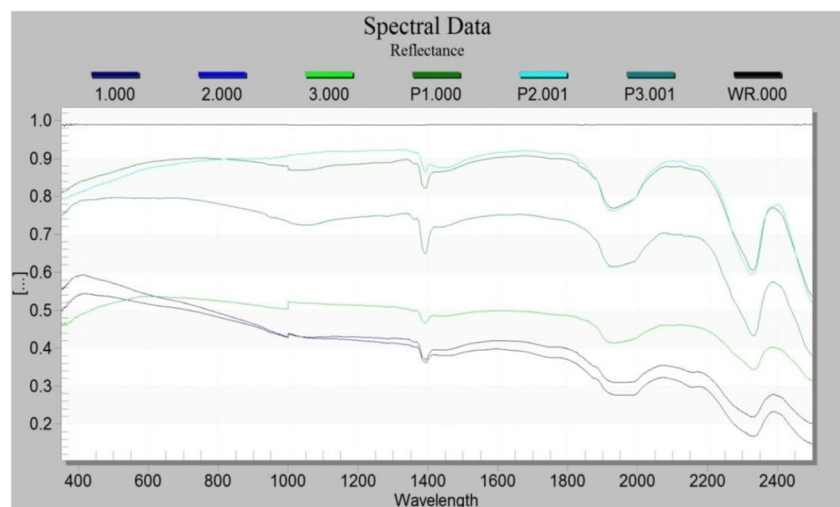


Fig. 6 Field spectra of limestone mineral

are established at Talaiyuttu. Narrow bands of coarse crystalline limestone also occur on the southern bank of Chittar river. Throughout its length, limestone is fine-grained with thin lenticular intercalations of coarse-grained, saccharoidal, compact and massive varieties. It is frequently intercalated with Quartzite bands. Bands of impure limestone and calciphyres have commonly occurred on the weathered surface. Very coarse and pure quality calcite (limestone) bands and pockets occur only at the southern end, but their extent is small and distribution is irregular. The major part of the band appears to be highly siliceous owing to close association with Quartzite. Limestone has various applications such as building material, aggregate as roads and etc. Figure 2 shows the limestone mineral and its spectral reflectance plot. Table 1 shows that the various satellite images are used and their specification.

Fig. 7 Endmember of purest limestone minerals

Methodology

The important objective of the present study examines the classification accuracy between Hyperion and Landsat-8 OLI imageries. Figure 3 shows the exhaustive methodology flowchart to identify the limestone mineral deposit.

The methodology adopted to the present research work is categorized into three groups. (i) Geochemical analysis. (ii) Field survey and sampling analysis using spectroradiometer. (iii) Processing of Hyperion data and Landsat-8 OLI imagery. In the Manur area, limestone samples are collected using GPS. The samples are converted as conductive materials by applying the carbon coating in limestone powder samples (Sun et al. 2011). The high-resolution imagery obtained by the electron beam applied on the limestone powder surface. The chemical components present in the limestone are identified

Table 2 List of unused bands in Hyperion sensor

S.No	Bad bands	Reason
1	1–7	Zero bands, non-illuminated
2	58–76	Zero bands, overlap region between VNIR-SWIR region
3	121–132	Water vapor region has lot of noise
5	165–181	Water vapor region has lot of noise
6	221–224	Water vapor region has lot of noise
7	225–242	Zero bands, non-illuminated

using the EDS method. Spectroradiometer generates the spectral characteristics of limestone that depends on the physical, chemical and optical properties (Honkavaara et al. 2012). In the processing of hyperspectral data, it involves data preprocessing, atmospheric correction, data dimensionality reduction, extraction of endmember spectra and limestone abundance estimation (Kruse et al., 2012). A total of 242 bands are available in Hyperion imagery; out of 242, 163 bands are in standardized conditions, because some of the bands in the Hyperion data have no data due to non-illuminated and overlap region and are present in 1–7, 58–76, 225–242 bands (Kumar and Yarrakula 2017). Hyperion data also contain bad bands; these bands are having a lot of noise and water vapor in the spectral region. The water vapor present in the bands is 120–132, 165–182, 221–224 (Scheffler and Karrasch 2013). Hyperion has a number of dark and bright columns due to change in the calibration or failure of capturing in CCD array. The vertical strip columns in Hyperion imagery were removed using a local destriping algorithm (Tsai et al., 2005). The radiance conversion of Hyperion imagery and Landsat-8 OLI imagery has done in Band Interleaved by Line format at the scale factor of 0.1. In the various atmospheric correction modules such as ACRON, QUAC, Flat field etc., FLAASH generates the smooth reflectance curve compared to other modules (Kumar and Yarrakula 2017). The absolute reflectance of both imageries obtained using FLAASH module. The

field spectra generated by the spectroradiometer given as input for classification (Lin et al. 2016). Spectral angle mapper (SAM) classification technique is taken to recognize the limestone mineral deposit in reflectance bands of both imageries.

Results and discussion

Chemical composition of limestone

In the Manur block, 14 limestone samples are collected. The geographical position of rock samples is developed using a global positioning system (GPS). Scanning electron microscopy (SEM) is used to identify the chemical composition of limestone mineral. The original limestone sample is made into two parts; part is used to generate the field spectra from ASD spectroradiometer and another part is used to identify the chemical composition in the limestone by making the powder samples. The limestone powder samples are converted as conductive materials by applying the carbon coating (Moroni et al. 2013). The high-resolution imagery obtained by the electron beam applied on the limestone powder surface. Figure 4 shows the high-resolution imagery of limestone achieved with SEM instrument.

To identify the Ca composition level and other chemical materials, EDS (energy dispersive X-ray spectroscopy) is performed. EDS allows identifying limestone mineral and those particular elements with relative proportions. Figure 5 shows the EDS graph with other elements present in the samples.

From the figure, it is observed that the weight percentage for C, O, Mg, Si and Ca are 46.68%, 39.86%, 1.48%, 0.24% and 11.73%, respectively. The atomic percentage for C, O, Mg, Si and Ca are 57.66%, 36.96%, 0.90%, 0.13% and 4.34%, respectively. In Fig. 5, it is clearly observed that the presence of CaCO_3 is high. Due to the presence of calcium carbonate content, deep absorption in the spectral curve is observed at 2000 nm.

Limestone spectra generation using ASD spectroradiometer

ASD spectroradiometer generates the field spectra in the visible, VNIR and SWIR regions. Limestone mineral samples are taken as the solid and powder material for spectroradiometer analysis. ASD produces the limestone spectra that depend on the physical, chemical and optical properties in a wavelength region between 400 and 2500 nm (Chuan et al. 2014).

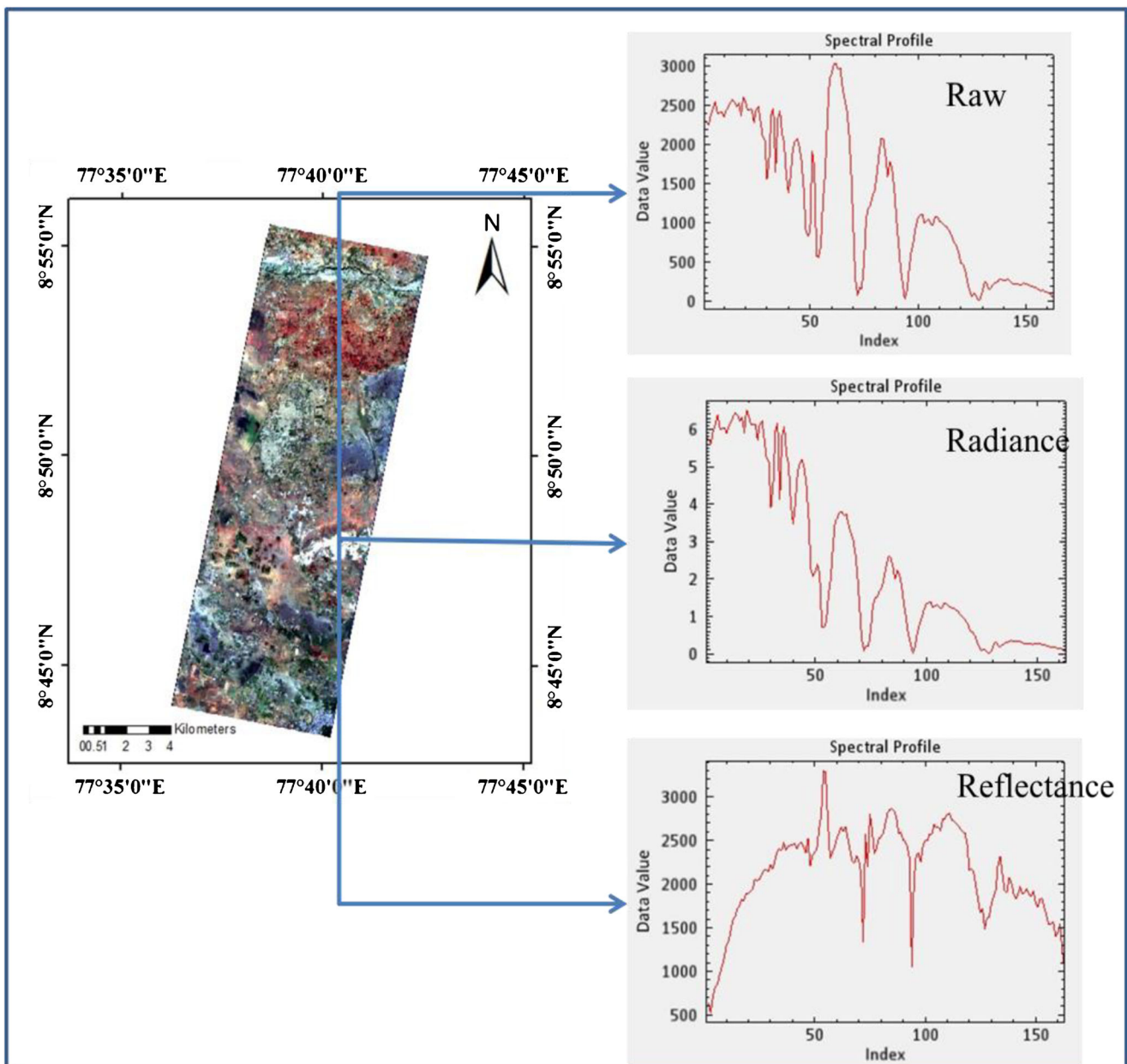
Due to the presence of carbonate, limestone spectra show deep absorption in the region of 1900 nm to 2050 nm. Figure 6 shows the ASD spectroradiometer

Table 3 List of strips present in Hyperion sensor

S.No	Band	Column
1	190	112
2	198	117
3	200	7
4	201	7
5	202	182
6	203	182
7	219	228

Table 4 Metadata information for FLAASH module

Scene center location—8°47'56" E and 77°39'51" N	Spectral polishing—no
Ground elevation—0.100 km	Use adjacency correction—yes
Sensor elevation—705 km	Wavelength recalibration—no
Pixel size—30 m	CO ₂ mixing ratio—390 ppm
Flight date—03 October 2015 time—03:34:52	Output reflectance scale factor—10,000
Atmospheric model—tropical	Use tile processing—no
Aerosol model: Rural-2 Band (K-T)	MODTRAN model—scaled DISORT
Water retrieval: yes—1130 nm	No. of DISTORT streams—8
Initial visibility—40 km	MODTRAN resolution—1 cm ⁻¹

**Fig. 8** Hyperion imagery and its spectral profile plot for raw image, radiance and reflectance

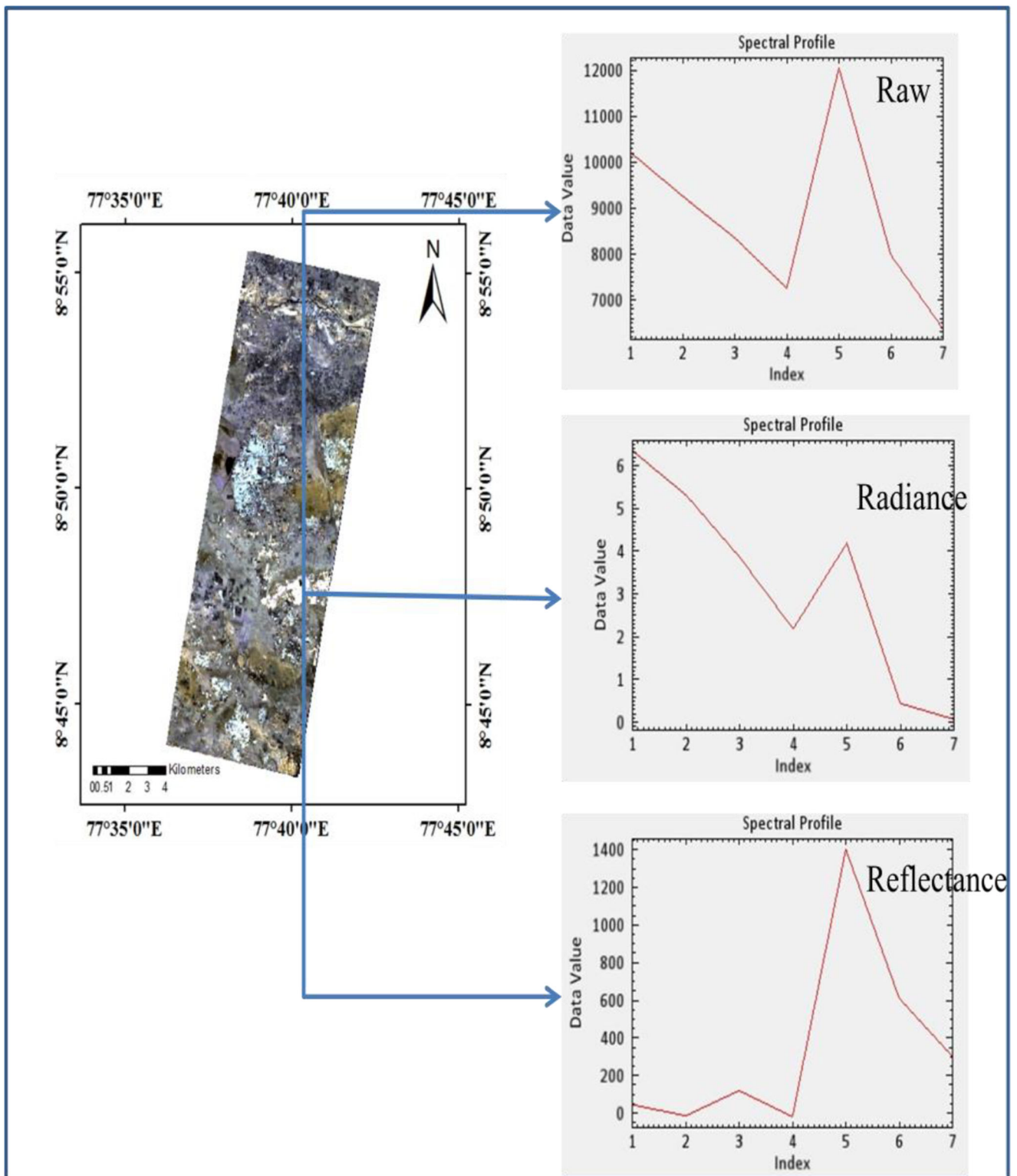
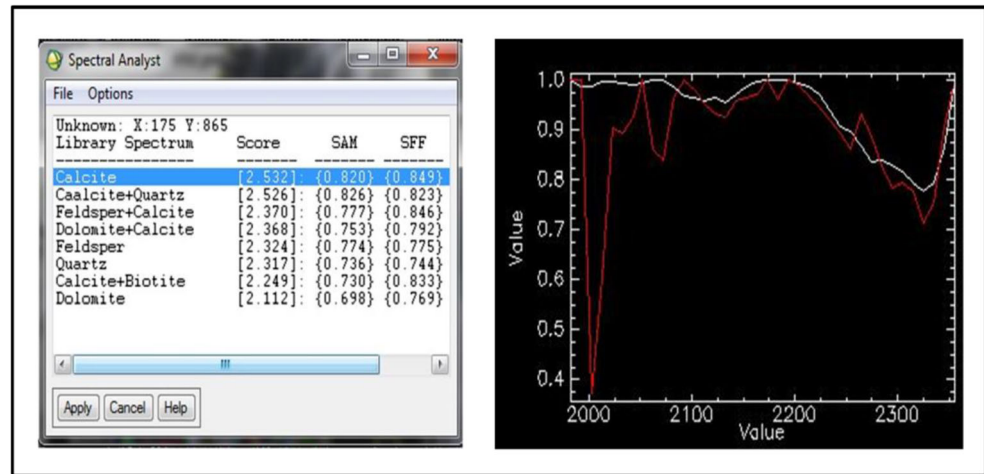


Fig. 9 Landsat-8 OLI imagery and its spectral profile plot for raw image, radiance and reflectance

and limestone mineral spectral curve. The red line curve indicates the limestone spectra and green line indicates the reference spectrum of the instrument. The raw spectra are

converted to field spectra such as various correction such as splice correction and etc. The field spectra of limestone samples are shown in Fig. 7.

Fig. 10 Field spectra comparison for limestone

Pre-processing of Hyperion and Landsat-8 OLI imagery

Removing the bad bands from Hyperion data

In Hyperion imagery, some bands contain no information, some bands contain heavy noise, this is called as bad bands. Hyperion data has a total of 242 bands, out of which 163 bands are in standardize condition, other bands are affected by noise, non-illuminated and water vapor (Kumar and Yarrakula 2017). Table 2 shows the list of unused and bad bands in the Hyperion sensor.

Destriping

In Hyperion CCD sensor array, particular column pixel values are a drop out then, visible as block line in the imagery. Vertical stripes are removed using several methods such as local destriping, global destriping, filtering techniques and morphological techniques. In the research work, SWIR region is only taken for the destriping process. The vertical strips present in the Hyperion data are removed using a local destriping algorithm and it is highly recommended for vertical stripe removal because it modifies striped column grey values

only (Kumar and Yarrakula 2017). Table 3 shows strips present in the SWIR region of Hyperion data.

In the present research work, the local destriping algorithm is used to remove the striping column by applying the nearest neighbourhood grey value averaging for the striped pixel and it is explained in equation 1.

$$\sum_{j=1}^n \frac{(x_{i-1,j,k}) + (x_{i+1,j,k})}{2n} \quad (1)$$

where i is the bad column, j is the line, k is the band, n is the number of pixels.

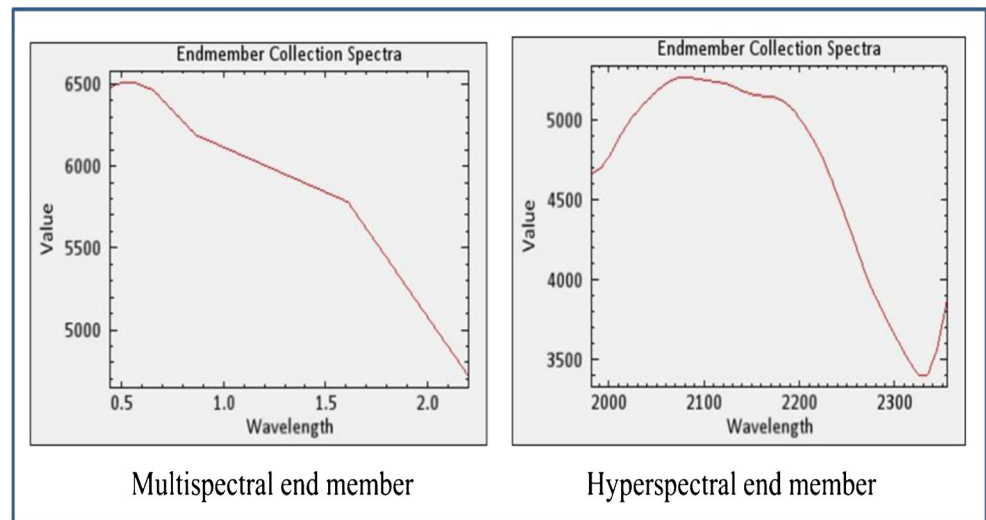
Absolute reflectance generation

The radiometric calibration generates the radiance value of the earth surface from the DN value of Hyperion data and Landsat-8 OLI data. The output file format is given as BIL (band interleaved by pixel) and a scale factor is taken as 0.1 (Kumar and Yarrakula 2017). The radiometric calibration converts the Hyperion CCD digital numbers to radiance value (Zaini et al. 2014). The absolute reflectance measurement designed to measure the absolute reflectance of a specular reflecting of rock samples. The reflectance of both imageries is performed using the FLAASH module. Using the absolute reflectance only, able to identify the Limestone deposit using field spectra. The input of FLAASH is radiometrically calibrated radiance image in BIL format. The data type is floating-point, 4-byte signed integers. FLAASH uses the advanced techniques to knob particularly straining atmospheric conditions, such as the occurrence of clouds. The absolute reflectance of both imageries is calculated using the FLAASH module accurately to compare other atmospheric modules (Kumar and Yarrakula 2017). FLAASH atmospheric correction module is used to get the spectral reflectance of each pixel in the optical imageries as precise manner. They utilize various parameters such as spectral polishing, sensor elevation,

Table 5 Probability scorer of samples

Mineral	SAM	SFF	BE	Total
Calcite	0.82	0.849	0.863	2.532
Calcite + biotite	0.811	0.878	0.748	2.437
Calcite + quartz	0.835	0.864	0.912	2.612
Dolomite + calcite	0.851	0.855	0.789	2.496
Feldspar + calcite	0.813	0.896	0.789	2.498

Fig. 11 Mean endmember for multispectral and hyperspectral imagery



wavelength recalibration, CO₂ mixing ratio, atmospheric model, the aerosol model, MODTRAN model, water retrieval, MODTRAN resolution and etc. Table 4 shows the metadata information for FLAASH module. Figure 8 shows the Hyperion imagery and its spectral profile plot of raw image, radiance and reflectance characteristics. Figure 9 shows the Landsat-8 OLI imagery and its spectral profile plot of raw image, radiance and reflectance characteristics.

Endmember generation

The limestone mineral spectra are obtained from the spectral libraries of USGS, JPL, JHU. The band interval of this mineral spectra is 2.5 nm, but the spectra interval of Hyperion imagery is 10 nm (El-magd et al. 2014). Spectral resembling methods are implemented to modify the library spectra information from 2.5 to 10 nm intervals. The spectral analyst tool

compares the limestone mineral library spectra to field spectra and produces probability using the methods such as spectral angle mapper (SAM), spectral feature fitting (SFF) and binary encoding (BE). Figure 10 shows the spectral comparison result of limestone. Table 5 describes the probability scorer of samples. Figure 11 shows the endmembers of Landsat-8 OLI and Hyperion imageries.

Spectral angle mapper

In the per-pixel based classification techniques, SAM provides superior classification results compared to other methods. The SAM method (equation 2) compares the image spectra and limestone spectra, and it manipulates the angular distance between the image spectrum and the limestone spectra.

Fig. 12 Limestone mapping in Landsat-8 OLI and Hyperion using SAM classification

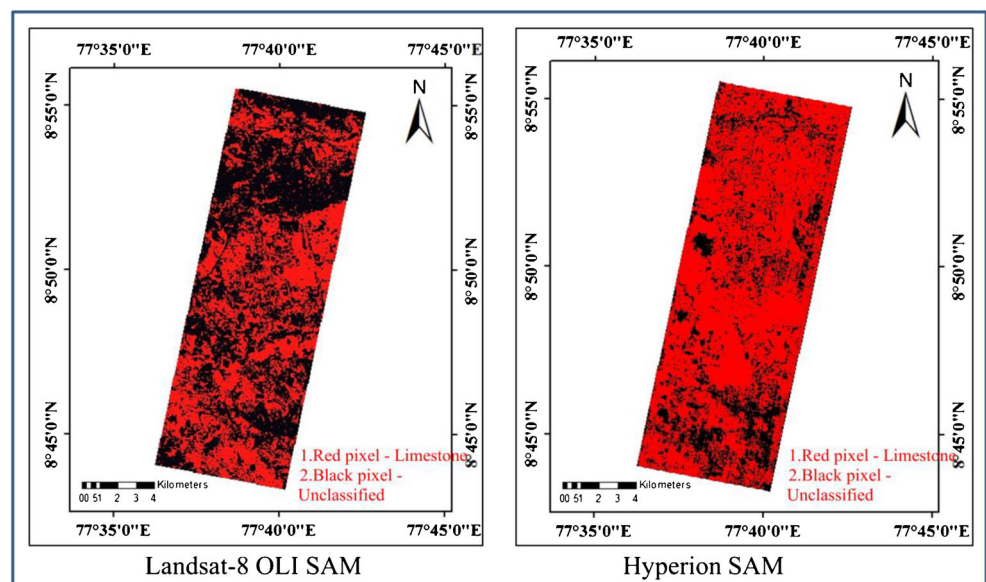


Table 6 Limestone deposit using Landsat-8 OLI and Hyperion imageries

Pixels	DN	Pixel count	Area (km ²)	Percent
Landsat-8 OLI Imagery Classification				
Unclassified	0	45,501	40.95	25.2469
Limestone	1	134,723	121.25	74.7531
Hyperion imagery classification				
Unclassified	0	83,444	75.10	46.28
Limestone	1	96,780	87.10	53.72

$$\alpha = \cos^{-1} \left(\frac{\sum_{i=1}^{nb} t_i r_i}{\left(\sqrt{\sum_{i=1}^{nb} t_i^2} \right) \left(\sqrt{\sum_{i=1}^{nb} r_i^2} \right)} \right) \quad (2)$$

where nb is the number of reflectance bands, t_i is the tested spectrum, r_i is the reference spectrum and α is the spectral angle. In the Hyperion imagery band, selection is taken from 1900 to 2400 nm in SWIR region around 38 bands. In the Landsat-8 OLI imagery, multispectral reflectance bands are taken around 7 bands. In the SAM classification, the field spectra utilized directly as the endmember spectrum for both imageries. The field spectrum and the reflectance imageries of both imageries are given as input for SAM classification. The basis angle is fixed using the trial and error method. Figure 12 shows the limestone classification using SAM in both imageries. The red pixels indicate the limestone deposits and the black pixels indicate the other earth surface information. The result of limestone deposit in both imageries is shown in Table 6.

Landsat-8 OLI imagery does not classify limestone clearly due to the large bandwidth between the reflectance bands. At the same time, Hyperion classifies the minerals accurately.

Conclusion

In the limestone chemical component such as calcium carbonate (CaCO₃), availability established using SEM and EDS analysis. The purest form of limestone spectral signatures is developed using ASD spectroradiometer for Indian climatic condition. The spectral curve of limestone shows the absorption in SWIR region around 2000 nm due to the carbonate content. Hyperion has 163 bands in standardized condition out of 242 bands, vertical strips are detached using a local destriping algorithm. Digital values of both imageries are converted to radiance at the scale factor of 0.1 in BIL format. The absolute reflectance values of Landsat-8 OLI and Hyperion imageries are obtained using the FLAASH correction module.

In both reflectance bands, limestone deposit is classified using SAM classification method. Due to large reflectance bands in short bandwidth intervals, Hyperion data classifies accurately than Landsat-8 OLI imagery. Based on the geochemical and optical properties, the purest limestone around 87.02 km² estimated for cement industries.

References

- Ahmadirouhani R, Karimpour MH, Rahimi B, Malekzadeh-Shafaroudi A, Pour AB, Pradhan B (2018) Integration of SPOT-5 and ASTER satellite data for structural tracing and hydrothermal alteration mineral mapping: implications for Cu–Au prospecting. *Int J Image Data Fusion* 9(3):237–262
- Arellano P, Tansey K, Balzter H, Boyd DS (2015) Detecting the effects of hydrocarbon pollution in the Amazon forest using hyperspectral satellite images. *Environ Pollut* 205:225–239
- Askari G, Pour A, Pradhan B, Sarfi M, Nazemnejad F (2018) Band ratios matrix transformation (BRMT): a sedimentary lithology mapping approach using ASTER satellite sensor. *Sensors* 18(10):3213
- Beiranvand Pour A, Park TY, Park Y, Hong J, Zoheir B, Pradhan B et al (2018) Application of multi-sensor satellite data for exploration of Zn–Pb sulfide mineralization in the Franklinian Basin, North Greenland. *Remote Sens* 10(8):1186
- Chuan Z, Fawang Y, Haixia H, Hongcheng L (2014) Study on the forest vegetation restoration monitoring using HJ-1A hyperspectral data. In *IOP Conference Series: Earth Environ Sci* 17(1):012082
- Crosta AP, de Souza Filho CR (2017) Hyperspectral remote sensing for mineral mapping: a case-study at alto Paraíso de Goiás, central Brazil. *Rev Bras Geosci* 30(3):551–554
- El-Magd IA, El Kafrawy S, Farag I (2014) Detecting oil spill contamination using airborne hyperspectral data in the River Nile, Egypt. *Open J Marine Sci* 4(2):140
- Honkavaara E, Kaivosoja J, Mäkinen J, Pellikka I, Pesonen L, Saari H et al (2012) Hyperspectral reflectance signatures and point clouds for precision agriculture by light weight UAV imaging system. *ISPRS Ann. Photogramm. Remote Sensing Spatial Inform Sci* 1-7: 353–358
- Kruse FA (2003) Mineral mapping with AVIRIS and EO-1 Hyperion. In: *Presented at the 12th JPL Airborne Geoscience Workshop*, 24–28 February, 2003. California, Pasadena
- Kruse FA, Bedell RL, Taranik JV, Peppin WA, Weatherbee O, Calvin WM (2012) Mapping alteration minerals at prospect, outcrop and drill core scales using imaging spectrometry. *Int J Remote Sens* 33(6):1780–1798
- Kruse, F. A and Boardman, J. W. (2000). Characterization and mapping of kimberlites and related diatremes using hyperspectral remote sensing. *Proceedings, 2000 IEEE Aerospace Conference.*, Big Sky, MO, March 18–24
- Kruse FA, Boardman JW, Huntington JF (2003) Comparison of airborne hyperspectral data and EO-1 Hyperion for mineral mapping. *IEEE Transac Geosci Remote Sensing* 41(6):1388–1400
- Kruse FA, Perry SL (2007) Regional mineral mapping by extending hyperspectral signatures using multispectral data. *IEEE Transac Geosci Remote Sensing* 4:1–14
- Kumar MV, Yarrakula K (2017) Comparison of efficient techniques of hyper-spectral image preprocessing for mineralogy and vegetation studies. *Ind J Geomarine Sci* 46:1008–1021
- Kumari SK, Debashish C, Pulakesh D, Jatisankar B (2014) Hyperion image analysis for iron ore mapping in Gua Iron Ore Region. *Int Res J Earth Sci* 2:1–6

- Lin L, Wang Y, Teng J, Wang X (2016) Hyperspectral analysis of soil organic matter in coal mining regions using wavelets, correlations, and partial least squares regression. *Environ Monit Assess* 188(2):97
- Matar SS, Bamoussa AO (2013) Integration of the ASTER thermal infrared bands imageries with geological map of Jabal Al Hasir area, Asir Terrane, the Arabian Shield. *J Taibah Univer Sci* 7(1):1–7
- Moroni M, Lupo E, Marra E, Cenedese A (2013) Hyperspectral image analysis in environmental monitoring: setup of a new tunable filter platform. *Procedia Environ Sci* 19:885–894
- Noori L, Pour AB, Askari G, Taghipour N, Pradhan B, Lee CW, Honarmand M (2019) Comparison of different algorithms to map hydrothermal alteration zones using ASTER remote sensing data for polymetallic vein-type ore exploration: Toroud–Chahshirin Magmatic Belt (TCMB), North Iran. *Remote Sens* 11(5):495
- Panda S, Banerjee K, Jain MK (2014) Mapping of iron minings of Noamundi Areas, Jharkhand by using the image based Ndi and Geospatial Technology. *Int J Innovation Sci Res* 7:5–10
- Peng, H. (2014). Automatic Denoising and Unmixing in Hyperspectral image processing. Rochester Institute of Technology
- Pour BA, Hashim M, van Genderen J (2013) Detection of hydrothermal alteration zones in a tropical region using satellite remote sensing data: Bau gold field, Sarawak. *Malay Ore Geol Rev* 54:181–196
- Ramakrishnan D, Nithya M, Singh KD, Bharti R (2013) A field technique for rapid lithological discrimination and ore mineral identification: results from Mamandur Polymetal Deposit, India. *J Earth System Sci* 122(1):93–106
- Renaud, K.M. (2015). Minerals yearbook
- Scheffler D, Karrasch P (2013) Preprocessing of hyperspectral images: a comparative study of destriping algorithms for EO1-Hyperion. In *SPIE Remote Sensing*. International Society for Optics and Photonics, p 88920
- Sheikhrasimi A, Pour AB, Pradhan B, Zoheir B (2019) Mapping hydrothermal alteration zones and lineaments associated with orogenic gold mineralization using ASTER data: a case study from the Sanandaj-Sirjan zone, Iran. *Adv Space Res* 63(10):3315–3332
- Sun Z, Zhao Y, Yan G, Li S (2011) Study on the hyperspectral polarized reflection characteristics of oil slicks on sea surfaces. *Chin Sci Bull* 56(15):1596–1602
- Tiwari SK, Saha SK, Kumar S (2015) Prediction modeling and mapping of soil carbon content using artificial neural network, hyperspectral satellite data and field spectroscopy. *Adv Remote Sens* 4(01):63
- Tsai, F., Lin, S. Q., Rau, J. Y., Chen, L. C., & Liu, G. R. (2005). Destriping hyperion imagery using spline interpolation. In *Proc. 26th Asian Conference on Remote Sensing*
- Yarrakula K, Deb D, Samanta B (2013) Comparative evaluation of Cartosat-1 and SRTM imageries for digital elevation modelling. *Geo-spatial Inform Sci* 16(2):75–82
- Zaini N, van der Meer F, van der Werff H (2014) Determination of carbonate rock chemistry using laboratory-based hyperspectral imagery. *Remote Sens* 6(5):4149–4172
- Zhang L, Du B (2012) Recent advances in hyperspectral image processing. *Geo-spatial Inform Sci* 15(3):143–156